NANO LETTERS

pubs.acs.org/NanoLett Letter

Synthesis of Lead-Free Cs_2AgBiX_6 (X = Cl, Br, I) Double Perovskite Nanoplatelets and Their Application in CO_2 Photocatalytic Reduction

Zhenyang Liu, Hanjun Yang, Junyu Wang, Yucheng Yuan, Katie Hills-Kimball, Tong Cai, Ping Wang, Aiwei Tang,* and Ou Chen*

Cite This: *Nano Lett.* 2021, 21, 1620−1627 Read Online

ACCESS | Metrics & More | Article Recommendations | Supporting Information

ABSTRACT: Morphology control represents an important strategy for the development of functional nanomaterials and has yet to be achieved in the case of promising lead-free double perovskite materials so far. In this work, high-quality Cs_2AgBiX_6 (X = Cl, Br, I) two-dimensional nanoplatelets were synthesized through a newly developed synthetic procedure. By analyzing the optical, morphological, and structural evolutions of the samples during synthesis, we elucidated that the growth mechanism of lead-free double perovskite nanoplatelets followed a lateral growth process from mono-octahedral-layer (half-unit-cell in thickness) cluster-based nanosheets to multilayer (three to four unit cells in thickness) nanoplatelets. Furthermore, we demonstrated that $Cs_2AgBiBr_6$ nanoplatelets possess a better performance in photocatalytic CO_2 reduction compared with their nanocube counterpart. Our work demonstrates the first example with two-dimensional morphology of this important class of lead-free perovskite materials, shedding light on the synthetic manipulation and the application integration of such promising materials.

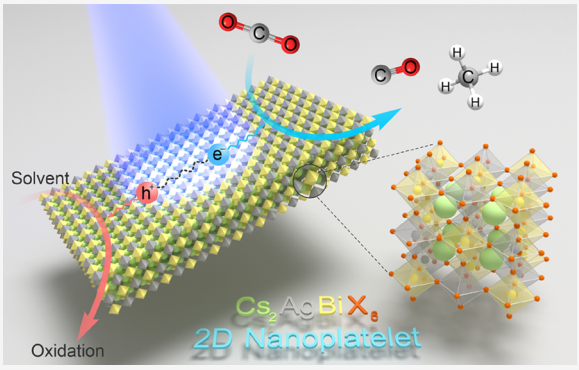

KEYWORDS: *Lead-free perovskite, Morphology control, 2D materials, Photocatalytic reaction, CO_2 reduction*

INTRODUCTION

Lead halide perovskite (LHP) nanocrystals have attracted a tremendous amount of interest in the past decade due to their excellent optical and optoelectronic properties, including high-photoluminescence quantum yields (PL QYs), low exciton binding energies, and long photocarrier diffusion lengths, *etc.*[1−5] These superior properties, accompanied by low-cost solution processability, render them extremely promising materials in a wide range of applications.[6−16] Despite these advantages, stability and toxicity (induced by lead inclusion) of LHP materials are the two major obstacles limiting their future applications.[17,18] In response, great efforts have been devoted to finding stable and non- or low-toxic alternatives.[19−24] In 2018, Creutz *et al.* and Locardi *et al.* first reported the syntheses of $Cs_2AgBiCl_6$ and $Cs_2AgInCl_6$ double perovskite nanocrystals, respectively.[25,26] Following these seminal works, to date, high-quality lead-free double perovskite nanocrystals with controllable, uniform sizes and superior optical and electronic properties have been demonstrated with greatly enhanced particle and crystal structure stabilities.[27−34] These high-quality double perovskite nanocrystals have been successfully integrated into a wide spectrum of applications, including solar cell devices,[27] ultraviolet and X-ray detectors,[35,36] photocatalytic reactions,[37] and light emitting diodes (LEDs),[34] *etc.*[38−40]

Morphology control of perovskite nanocrystals is an imperative strategy to further tune and improve the materials' performance in applications.[41−45] This strategy has been extensively explored for LHP nanocrystals, with successful demonstrations of different particle morphologies, *i.e.*, 0D nanocubes (NCs),[46,47] 1D nanorods/nanowires,[44,48] and 2D nanosheets/nanoplatelets (NPLs).[49−51] In particular, 2D perovskite NPLs show unique chemical and physical properties such as anisotropically quantum-confined photocarriers, unified exposed crystal facet, defined surface atomic arrangement/symmetries, and superior performances as substrates/supports in nanocomposites.[52−56] Those advantages impart great potentials to perovskite NPLs for a number of applications, especially for photocatalytic reactions including,

Received: October 16, 2020
Revised: February 4, 2021
Published: February 11, 2021

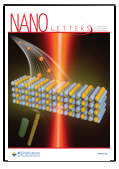

Downloaded via BROWN UNIV on February 26, 2021 at 19:38:35 (UTC).
See https://pubs.acs.org/sharingguidelines for options on how to legitimately share published articles.

ACS Publications © 2021 American Chemical Society

https://dx.doi.org/10.1021/acs.nanolett.0c04148
Nano Lett. 2021, 21, 1620−1627

CO_2 reduction and water splitting. Despite these promises, morphology control in lead-free double perovskite nanomaterials has rarely been studied and double perovskite NPLs are yet to be realized, signifying an urgent need for developing new synthetic chemistries for a family of such promising materials.

Herein, we report the first colloidal synthesis of Cs_2AgBiX_6 2D NPLs through a new synthetic route involving a room-temperature precursor injection followed by a solution heating-up process. The as-prepared NPLs were well-characterized, and the growth mechanism was investigated by sampling the reaction at different stages. The mechanistic study showed that thin $Cs_2AgBiBr_6$ nanosheets containing a half-unit-cell layer along the vertical direction were initially formed. The subsequent heating process allowed for the growth of thin monolayer nanosheets into multilayer (three to four unit-cell layers) thick NPLs with a well-defined rectangular shape and improved crystallinity. Moreover, we demonstrated that direct-synthetic halide compositional tuning of Cs_2AgBiX_6 double perovskite NPLs is feasible, highlighting an alternative method for control over the NPL properties. Further, we applied the as-synthesized $Cs_2AgBiBr_6$ double perovskite NPLs as an efficient photocatalyst for CO_2 reduction reactions under visible light illumination. Our study reported here not only provides an effective means to access high-quality double perovskite NPLs but also sheds light on future explorations of morphologically controlled lead-free perovskite materials for a wide spectrum of applications with enhanced performances.

RESULT AND DISCUSSION

The synthetic route of lead-free Cs_2AgBiX_6 double perovskite NPLs is shown in Figure 1. In a typical synthesis of $Cs_2AgBiBr_6$

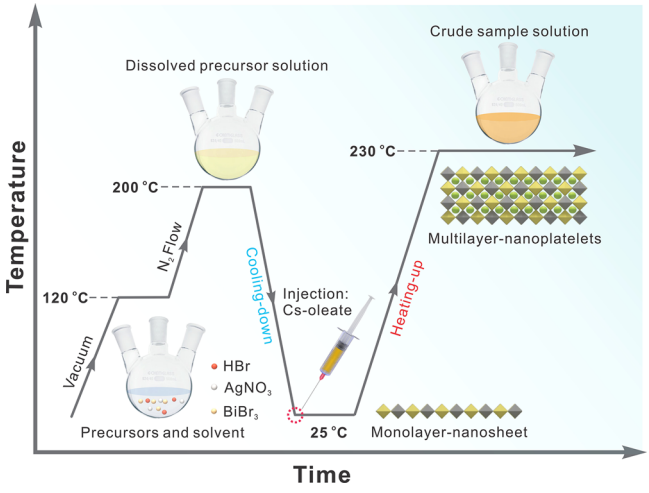

Figure 1. Schematic illustration of the synthetic procedure of lead-free $Cs_2AgBiBr_6$ double perovskite 2D NPLs.

NPLs, after all of the chemicals (*i.e.*, $BiBr_3$, $AgNO_3$, HBr, oleic acid, oleylamine, and 1-octadecene) were loaded into the flask, the system was degassed at 120 °C followed by heating to 200 °C under N_2 protection to make a homogeneous solution (Figure 1). Subsequently, the reaction solution was cooled to room temperature and a Cs-oleate precursor solution was injected to induce the nucleation of $Cs_2AgBiBr_6$ cluster-based nanosheets. The reaction solution was then reheated to 230 °C for 10 min, during which, multilayer NPLs were produced (Figure 1). This growth mechanism will be discussed in further detail below.

The absorption spectrum of the obtained $Cs_2AgBiBr_6$ NPLs showed two absorption bands at 355 nm (3.50 eV) and 438 nm (2.84 eV) (Figure 2A), which is consistent with previous reports on the $Cs_2AgBiBr_6$ double perovskite materials with an indirect band gap nature.[57,58] To accurately determine the band gap energy, diffused reflectance measurements of the $Cs_2AgBiBr_6$ NPL powders were carried out (see details in the Supporting Information (SI), Figure S1).[29] The band gap was determined to be 2.06 eV by a Tauc plot analysis assuming indirect allowed transition (Figure S2). This band gap energy is slightly larger than the bulk material (~1.95 eV),[21,57] indicating its weak quantum confinement.[29] The $Cs_2AgBiBr_6$ NPLs exhibited a broad weak photoluminescence (PL) peak centered at ~640 nm (~1.94 eV) with a full width at half-maximum (fwhm) of 143 nm (427 meV), which is in accordance with previous reports of $Cs_2AgBiBr_6$ double perovskite NCs (Figure 2A).[36] The large Stokes shift and broad emission peak signified a self-trapped emission mechanism.[58,59] A typical transmission electron microscopy (TEM) image of the $Cs_2AgBiBr_6$ NPLs depicted a rectangular morphology with an average edge length of 180 ± 130 nm (Figure 2B, Figures S3 and S4). Low and similar image contrasts of individual NPLs indicated a relatively thin and uniform NPL thickness (Figure 2B). High-resolution TEM (HR-TEM) measurements revealed a high crystallinity of individual NPLs with lattice fringes across the entire platelets (Figure 2C). Clear visualizations of lattice *d*-spacings of 3.9 and 2.8 Å can be assigned to the (220) and (400) planes of the cubic double perovskite crystal phase (space group, $Fm\bar{3}m$), respectively (Figure 2C).[60] The corresponding fast Fourier transform (FFT) pattern of the image confirmed the cubic phase of the NPL, consistent with the computer-simulated electron diffraction pattern along the [001] projection of the double perovskite crystal lattice (Figure 2C, right panels).[61] Atomic force microscopy (AFM) measurements suggested that the thickness of the obtained $Cs_2AgBiBr_6$ NPLs was between 3.6 and 6.0 nm (Figure 2D,E), which corresponded to three to five unit-cell layers in the normal direction along the [001] crystallographic axis (11.3 Å for each unit cell, Figure S5).[60] The XRD pattern of the as-prepared $Cs_2AgBiBr_6$ NPLs unambiguously confirmed the double perovskite crystal phase with all of the Bragg diffraction peaks matching well with reported bulk $Cs_2AgBiBr_6$ double perovskite (Figure 2F).[21,60] An average lattice parameter (*a*) of 11.29 Å was calculated on the basis of the major Bragg diffraction peaks shown in Figure 2F (Table S1), matching well to the lattice parameter of bulk $Cs_2AgBiBr_6$ double perovskite (*a* = 11.27 Å from ICSD Coll. Code 230901). The relatively high intensity for the (400) diffraction peak indicated a preferred orientation of the NPLs, in good agreement with the stacking of laterally laid NPLs parallel to the substrate (Figure 2F inset).[62] To further validate the orientation alignment and 2D morphology of the material, a sample of fully oriented $Cs_2AgBiBr_6$ NPLs on a XRD substrate was carefully prepared (see details in the SI), and only showed a set of enhanced {*l*00} peaks in the XRD pattern (Figure S6).[62] Scanning electron microscopy energy dispersive X-ray spectroscopy (SEM-EDS) measurements showed colocalized signals for all of the elements in the $Cs_2AgBiBr_6$ NPLs with an atomic ratio of Cs:Ag:Bi:Br = 1.9:0.9:1.0:6.2, in agreement with the standard stoichiometry of 2:1:1:6 (Figure S7, Table S2). In addition, we found that by introducing different amounts of octylamine in addition to the added oleylamine, the lateral dimension of the resultant NPLs can be

https://dx.doi.org/10.1021/acs.nanolett.0c04148
Nano Lett. 2021, 21, 1620−1627

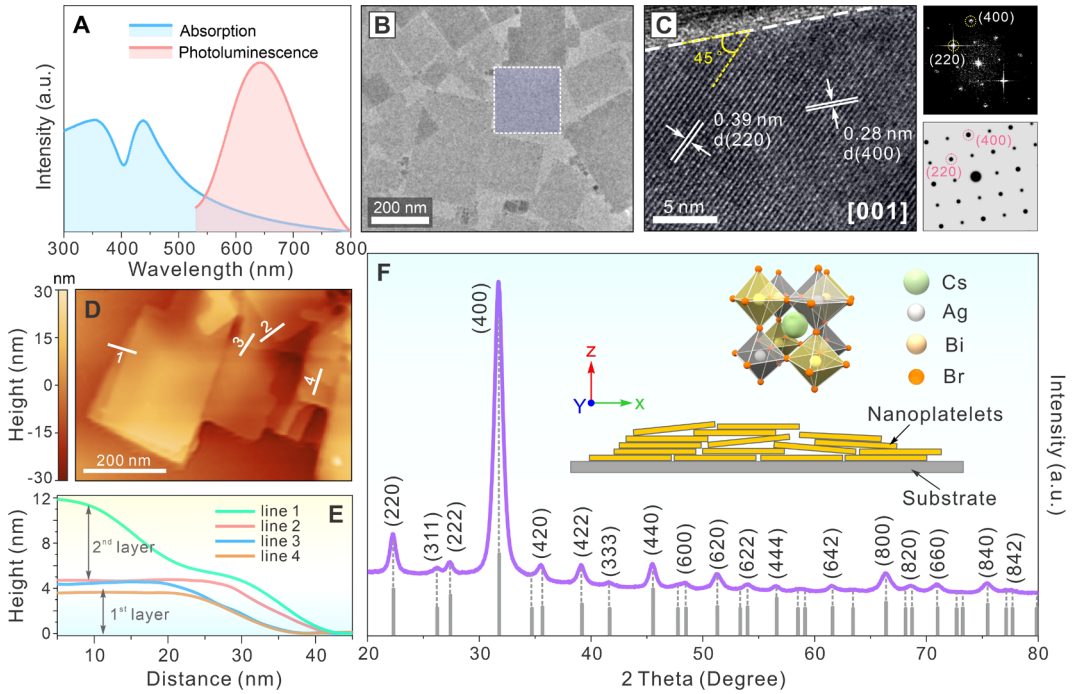

Figure 2. (A) Absorption (blue) and PL (pink) spectra of as-prepared $Cs_2AgBiBr_6$ NPLs in a toluene solution. (B, C) Typical TEM image (B, highlighted by dashed square) and a HR-TEM image (C) of the $Cs_2AgBiBr_6$ NPLs. The right top panel in panel C is the FFT pattern of the HR-TEM image, and the right bottom panel is the simulated FFT pattern along the [001] projection of the $Cs_2AgBiBr_6$ double perovskite crystal phase. (D, E) AFM image (D) and the corresponding height analysis (E) of the $Cs_2AgBiBr_6$ NPLs. (F) XRD pattern of the $Cs_2AgBiBr_6$ NPLs. The gray bars show the standard XRD peak positions for bulk $Cs_2AgBiBr_6$ double perovskite (ICSD Coll. Code: 230901). The insets are schematic images representing the platelet preferred orientation effect and schematic of $Cs_2AgBiBr_6$ double perovskite crystal unit cell.

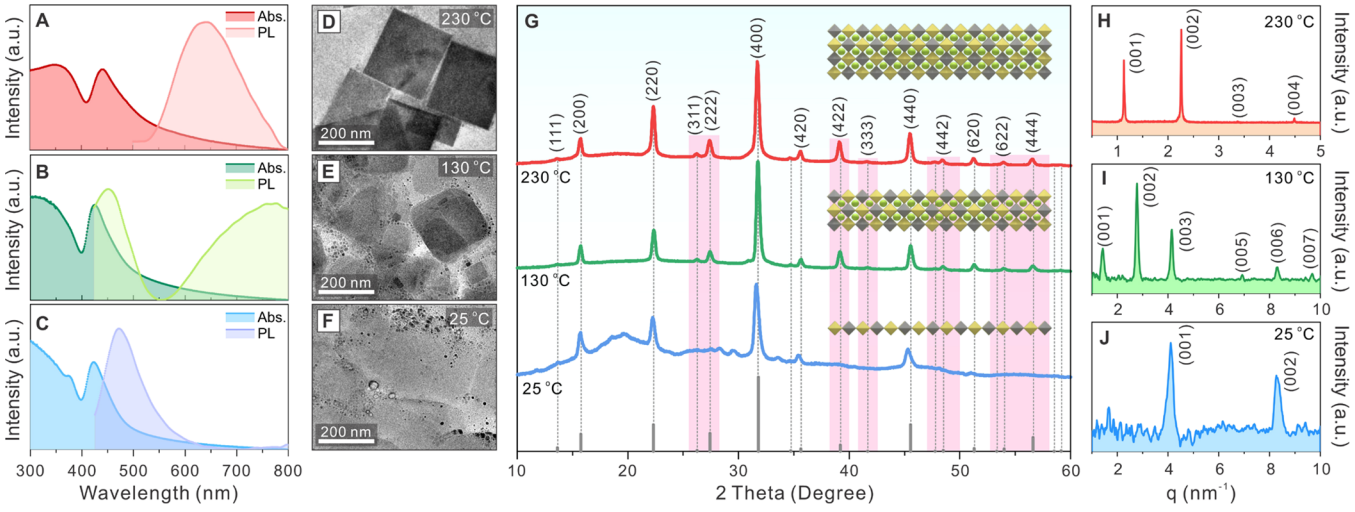

Figure 3. (A–F) Absorption and PL spectra (A–C) and the corresponding TEM images (D–F) of the samples collected at different reaction stages during the synthesis of the $Cs_2AgBiBr_6$ double perovskite NPLs. (G) Corresponding XRD patterns of the samples shown in panels A–F. Insets are the schematic illustrations of the formation process of $Cs_2AgBiBr_6$ double perovskite NPLs. (H–J) Corresponding SAXS patterns of the samples collected at different reaction stages.

controlled.[49,51] By varying the volume ratio of octylamine and oleylamine from 2:8 to 8:2 (while maintaining the total volume at 1 mL) while keeping other reaction conditions constant, the lateral size of the NPLs could be tuned from ~330 ± 230 to 630 ± 380 nm without disturbing the double perovskite crystal structure (see the SI for details, Figures S8 and S9).

To investigate the formation mechanism of the $Cs_2AgBiBr_6$ double perovskite NPLs, we monitored the optical properties, particle morphology, and structural evolutions through sampling the reaction at different stages during the synthetic process (Figure 3). The absorption spectrum of the sample collected at 25 °C after injection of Cs-oleate precursor showed an absorption peak at 420 nm along with a small absorption feature at 375 nm (Figure 3C). While the small absorption feature appeared before Cs-oleate injection and was likely due to the presence of unreacted precursors (*i.e.*, $[BiBr_6]^{3-}$ complexes, Figure S10),[63−65] the major absorption peak (~420 nm) is a characteristic of $Cs_2AgBiBr_6$ double

https://dx.doi.org/10.1021/acs.nanolett.0c04148
Nano Lett. 2021, 21, 1620−1627

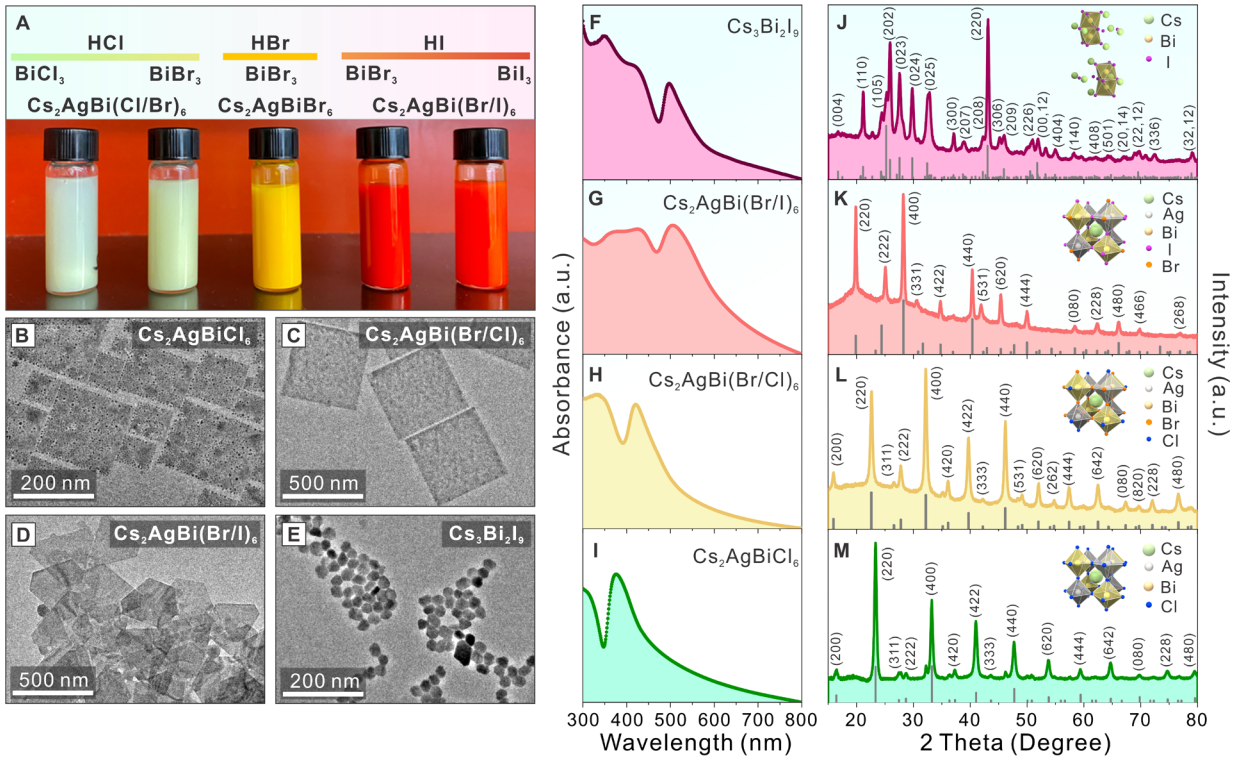

Figure 4. (A) Photographs and the required halide−precursor combinations for the samples with different halide compositions. (B−E) TEM images of the Cs_2AgBiX_6 double perovskite NPLs with different halide compositions (B−D) and $Cs_3Bi_2I_9$ nanoparticles (E). (F−M) Corresponding absorption spectra (F−I) and XRD patterns (J−M) for the samples shown in panels B−E.

perovskites.[25,31,57] A weak emission peak centered at 475 nm was observed (Figure 3C), which was independent of excitation wavelength (Figure S11), indicating that it is due to an electronic transition rather than a light scattering effect from the sample.[66] Such blue emission can only be assigned to the direct band gap exciton recombination of ultrathin $Cs_2AgBiBr_6$ double perovskite.[57] The formation of these ultrathin nanosheets was further confirmed by the measured TEM images with low image contrast. The irregular shapes of these $Cs_2AgBiBr_6$ nanosheets were likely caused by low temperature induced insufficient crystallization (Figure 3F).[21,67] Upon increasing the temperature to 130 °C, a new broad emission peak emerged at ∼750 nm (Figure 3B), attributing to the self-trapped emission from the $Cs_2AgBiBr_6$ double perovskites.[58,59] The band gap energies of 2.26 eV and 2.21 eV were determined by the Tauc plot analyses of the diffused reflectance measurements for the two samples collected at 25 and 130 °C, respectively (Figure S12). The slightly larger values than the band gap (2.06 eV) of the final $Cs_2AgBiBr_6$ NPLs (collected at 230 °C) indicated stronger exciton confinements due to smaller thicknesses of the nanosheets. A more defined NPL shape and increased image contrast compared to the sample at 25 °C further indicated the subsequent growth into relatively thick NPLs with improved crystallization (Figure 3E). When the temperature reached 230 °C, the emission peak located at 475 nm totally disappeared and the self-trapped emission peak blue-shifted to 640 nm (Figure 3A). While the disappearance of the 475 nm emission peak suggested that all of the thin nanosheets grew into thick NPLs, a significant blue shift (*i.e.*, from 750 to 640 nm) of the self-trapped emission peak indicated a full crystallization of the double perovskite structure of the resulting NPLs,[25,32,57] consistent with the TEM and XRD measurements (Figure 3D,G).

The growth mechanism from thin nanosheets to thick NPLs was further proved by XRD and small-angle X-ray scattering (SAXS) measurements. As depicted in Figure 3G, the XRD pattern for the ultrathin nanosheet sample collected at 25 °C (blue) matched well with the standard pattern of $Cs_2AgBiBr_6$ double perovskite except for the absence of all *Z*-direction-related Bragg diffraction peaks (*i.e.*, {*hkl*}, with $l \neq 0$, highlighted in pink). This XRD result strongly supported the formation of ultrathin $Cs_2AgBiBr_6$ nanosheets with only a half-unit-cell thickness along the vertical direction of the NPLs.[62] When increasing the reaction temperature to 130 and 230 °C, while the double perovskite crystal structure remained intact, all of the *Z*-direction-related diffraction peaks emerged in the measured XRD patterns (Figure 3G, green and red, respectively), indicating an increased NPL thickness and agreeing well with our proposed NPL growth mechanism. Furthermore, SAXS patterns of the three samples collected at different temperatures (*i.e.*, 25, 130, and 230 °C) showed a layered lamellar structure with an interlayer distance increasing from 1.53 to 5.58 nm upon increasing temperature (Figure 3H−J, Tables S3−S5), indicating the NPL thickness increased from half-unit-cells to three to four unit cells with considerations of the presence of bilayer organic ligands and their interdigitation between neighboring NPLs,[68] further validating the growth mechanism.

To expand the compositional space, we have synthesized Bi-based double perovskite NPLs with different halide compositions (Figure 4). By replacing Br-containing precursors (*i.e.*, $BiBr_3$ and HBr) with Cl-containing ones (*i.e.*, $BiCl_3$, and HCl) in the initial reaction solution while maintaining other reaction conditions, rectangular-shaped $Cs_2AgBiCl_6$ double perovskite

https://dx.doi.org/10.1021/acs.nanolett.0c04148
Nano Lett. 2021, 21, 1620−1627

NPLs with an average edge length of 120 ± 80 nm were obtained (Figure 4A,B and Figure S13A). In addition, when mixing Br-containing precursors and Cl-containing precursors with different molar ratios, mixed-halide $Cs_2AgBi(Br/Cl)_6$ NPLs can also be achieved (Figure 4A,C). For the I-containing cases, a mixture of Br-containing precursors and I-containing precursors (*i.e.*, BiI_3 and HI) accompanied by a lowered final reaction temperature of 100 °C were required for the synthesis of $Cs_2AgBi(Br/I)_6$ double perovskite NPLs (Figure 4A,D and Figure S13B). Higher reaction temperatures (>130 °C), however, resulted in the formation of $Cs_3Bi_2(Br/I)_9$ NPLs with a 2D layered crystal structure (space group, $P\bar{3}m1$), without the incorporation of any Ag (Figure S14).[63,64] However, a complete replacement of Br-containing precursors with I-containing ones led to the formation of $Cs_3Bi_2I_9$ nanoparticles with a 0D dimer-type crystal phase (space group, $P6_3/mmc$) featuring face-sharing $[Bi_2X_9]^{3-}$ units (Figure 4E,F,J),[69] suggesting the necessity of Br inclusion for stabilizing the double perovskite crystal structure.[64] Absorption spectra of the obtained Cs_2AgBiX_6 double perovskite NPLs with different halide compositions are shown in Figure 4G–I. An apparent red shift of the first absorption peak can be observed while tuning from Cl- to Br- and I-containing NPLs (Figure 4G–I), agreeing well with the trends observed for their cube-shaped counterparts.[25] XRD measurements confirmed the cubic double perovskite crystal structure for these samples. And all of the XRD peaks shifted to lower 2θ angles when the halide composition was tuned from Cl to Br to I (Figure 4K–M), which was attributed to the lattice expansion caused by increasing ionic radii (*i.e.*, Cl^-, 1.67 Å; Br^-, 1.81 Å; I^-, 2.06 Å).

Zhou *et al.* demonstrated that $Cs_2AgBiBr_6$ NCs can be used as photocatalyst in CO_2 reduction reaction, in which CO_2 saturated ethyl acetate was used as reaction solution.[37] Since 2D NPLs possess a high percentage of surface atoms, superior free-charge mobilities, and a short distance to surface catalytic sites, it is shown that the 2D morphology can greatly promote their performances in photocatalytic reactions.[42,56] To examine the photocatalytic performance of the obtained $Cs_2AgBiBr_6$ NPLs, we have carried out CO_2 photoreduction reactions using the $Cs_2AgBiBr_6$ NPLs as the catalyst (see the SI for experimental details). Nearly no H_2 can be detected throughout the entire reaction (Figure S15), suggesting that the selectivity for the CO_2 reduction was >99% with a total suppression of the possible H_2 evolution reaction under the current reaction conditions. The reaction mechanism is expected to be the same as that of the 0D $Cs_2AgBiBr_6$ double perovskite NCs,[37] in which the photogenerated charge carriers (*i.e.*, electron and hole) would dissociate in NPLs, following which the hole is consumed by solvent molecule (*e.g.*, ethyl acetate) while the electron can be captured by CO_2 (Figure 5A). To further confirm the photocatalytic role of the $Cs_2AgBiBr_6$ NPLs, three control experiments were conducted. The first and second control experiments were carried without the $Cs_2AgBiBr_6$ NPLs and light, respectively. The results showed more than 2 orders of magnitude lower production amounts for both CO and CH_4 (Figures S16 and S17), indicating that photogenerated charge carriers are responsible for the CO_2 reduction reaction. The third control experiment under N_2 atmosphere without CO_2 showed that a small amount of CO can be detected with the absence of CH_4 (Figure S18), proving the possible oxidization of solvent (ethyl acetate) as reported previously.[70] These three experiments

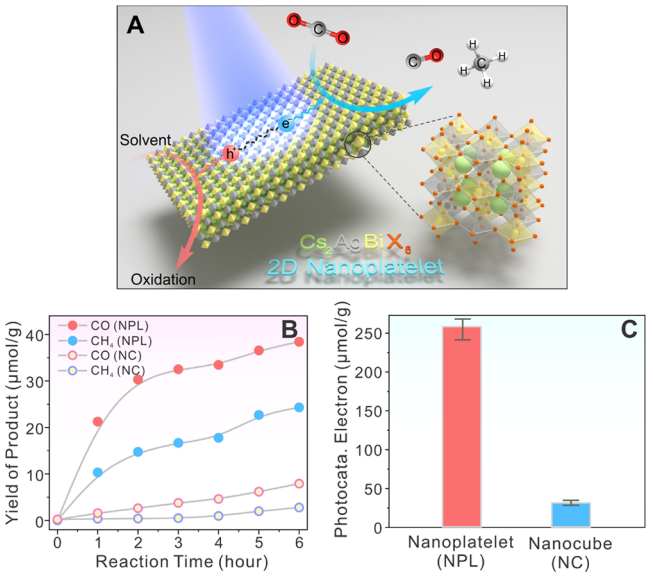

Figure 5. (A) Schematic illustration of the $Cs_2AgBiBr_6$ NPL photocatalyzed CO_2 reduction reaction. (B) CO (red) and CH_4 (blue) product yield evolutions as a function of reaction time for using $Cs_2AgBiBr_6$ double perovskite NPLs (solid) and NCs (open) as catalysts. (C) Histogram of the total photocatalytic electron consumption in 6 h for the reactions using $Cs_2AgBiBr_6$ double perovskite NPLs (red) and NCs (blue) as the catalysts.

supported the proposed mechanism, and more detailed studies are still ongoing.

To demonstrate the shape effect in the photocatalytic reaction, we have compared the photocatalytic performances of the $Cs_2AgBiBr_6$ NPLs and NCs. The same masses of inorganic components for the NPL and NC samples (calibrated by thermogravimetric analysis) were applied to the reaction under identical reaction conditions (see the SI for experimental details, Figures S19 and S20). As shown in Figure 5B, both the CO and CH_4 production rates were significantly higher when using the NPLs as catalysts compared to the NCs. However, the production rate gradually decreased with the prolonging of the reaction time, which may be due to some surface poisoning of the photocatalysts. The total electron consumption during the course of the reaction (*i.e.*, 6 h) for the $Cs_2AgBiBr_6$ NPLs showed a more than 8-fold enhancement compared to that of the $Cs_2AgBiBr_6$ NCs under the same reaction conditions (255.4 μmol/g *vs* 30.8 μmol/g, Figure 5C). Such a drastically improved photocatalytic performance was likely due to the anisotropically confined charge carries and their in-plane long diffusion length for the NPLs as compared to their NC counterparts.[71−74] Moreover, the average external quantum efficiency of the system during the 6 h reaction time was calculated to be 0.035% (see details in the SI). Remarkably, both the double perovskite crystal structure and the 2D morphology of the $Cs_2AgBiBr_6$ NPLs were maintained after the photoreaction (Figure S21), demonstrating the superior material stability.

■ CONCLUSION

In summary, we report a new synthetic route to achieve high-quality lead-free Cs_2AgBiX_6 (X = Cl, Br, I) double perovskite 2D NPLs. We show that the NPL formation process follows a unique growth mechanism, in which Cs_2AgBiX_6 mono-octahedral-layer cluster-based nanosheets are first synthesized

https://dx.doi.org/10.1021/acs.nanolett.0c04148
Nano Lett. 2021, 21, 1620−1627

at room temperature, followed by their growth into multilayer-thick NPLs at a higher reaction temperature. By controlling the halide composition, we have successfully synthesized a series of double perovskite NPLs with different halide compositions and their combinations. Further, we show that the as-synthesized $Cs_2AgBiBr_6$ NPLs can serve as efficient photocatalysts for CO_2 photoreduction. Our work not only conveys the first demonstration of morphology control in lead-free double perovskite materials but may also guide future efforts in the synthetic designs and applications of lead-free perovskite and perovskite-analogue materials in general.

■ ASSOCIATED CONTENT

Supporting Information

The Supporting Information is available free of charge at https://pubs.acs.org/doi/10.1021/acs.nanolett.0c04148.

Additional experimental details, EQE calculations details of photocatalytic CO_2 reduction reaction, calculations of cell parameter for as prepared NPLs, edge size distribution, XRD analysis, SEM-EDS results, TEM, PL, and absorption spectrum (PDF)

■ AUTHOR INFORMATION

Corresponding Authors

Aiwei Tang − *Key Laboratory of Luminescence and Optical Information Ministry of Education, School of Science, Beijing Jiaotong University, Beijing 100044, China;* orcid.org/0000-0002-0716-0387; Email: awtang@bjtu.edu.cn

Ou Chen − *Department of Chemistry, Brown University, Providence, Rhode Island 02912, United States;* orcid.org/0000-0003-0551-090X; Email: ouchen@brown.edu

Authors

Zhenyang Liu − *Department of Chemistry, Brown University, Providence, Rhode Island 02912, United States; Key Laboratory of Luminescence and Optical Information Ministry of Education, School of Science, Beijing Jiaotong University, Beijing 100044, China*

Hanjun Yang − *Department of Chemistry, Brown University, Providence, Rhode Island 02912, United States*

Junyu Wang − *Department of Chemistry, Brown University, Providence, Rhode Island 02912, United States*

Yucheng Yuan − *Department of Chemistry, Brown University, Providence, Rhode Island 02912, United States;* orcid.org/0000-0003-3935-0967

Katie Hills-Kimball − *Department of Chemistry, Brown University, Providence, Rhode Island 02912, United States*

Tong Cai − *Department of Chemistry, Brown University, Providence, Rhode Island 02912, United States;* orcid.org/0000-0002-4468-6767

Ping Wang − *Department of Chemistry, Brown University, Providence, Rhode Island 02912, United States; State Key Laboratory of Electroanalytical Chemistry, Changchun Institute of Applied Chemistry, Chinese Academy of Sciences, Changchun 130022, Jilin, China;* orcid.org/0000-0002-7189-9418

Complete contact information is available at: https://pubs.acs.org/10.1021/acs.nanolett.0c04148

Funding

O.C. acknowledges support from the Brown University startup funds and the Alfred P. Sloan Foundation through the Sloan Research Fellowship program. O.C. also acknowledges support from the National Science Foundation through the NSF CAREER program (Grant DMR-1943930) and CBET program (Grant CBET-1936223).

Notes

The authors declare no competing financial interest.

■ ACKNOWLEDGMENTS

O.C. acknowledges support for SEM-EDS, TEM, AFM, and XRD measurements performed at the Electron Microscopy Facility in the Institute for Molecular and Nanoscale Innovation (IMNI) at Brown University. Z.L. acknowledges the support from the China Scholarship Council.

■ REFERENCES

(1) Kojima, A.; Teshima, K.; Shirai, Y.; Miyasaka, T. Organometal Halide Perovskites as Visible-light Sensitizers for Photovoltaic Cells. *J. Am. Chem. Soc.* **2009**, *131* (17), 6050−6051.

(2) Lee, M. M.; Teuscher, J.; Miyasaka, T.; Murakami, T. N.; Snaith, H. J. Efficient Hybrid Solar Cells Based on Meso-Superstructured Organometal Halide Perovskites. *Science* **2012**, *338* (6107), 643−647.

(3) Burschka, J.; Pellet, N.; Moon, S. J.; Humphry-Baker, R.; Gao, P.; Nazeeruddin, M. K.; Gratzel, M. Sequential Deposition as a Route to High-Performance Perovskite-Sensitized Solar Cells. *Nature* **2013**, *499* (7458), 316−319.

(4) Stranks, S. D.; Eperon, G. E.; Grancini, G.; Menelaou, C.; Alcocer, M. J.; Leijtens, T.; Herz, L. M.; Petrozza, A.; Snaith, H. J. Electron-Hole Diffusion Lengths Exceeding 1 Micrometer in an Organometal Trihalide Perovskite Absorber. *Science* **2013**, *342* (6156), 341−344.

(5) Jeon, N. J.; Noh, J. H.; Yang, W. S.; Kim, Y. C.; Ryu, S.; Seo, J.; Seok, S. I. Compositional Engineering of Perovskite Materials for High-Performance Solar Cells. *Nature* **2015**, *517* (7535), 476−480.

(6) Chen, W.; Wu, Y.; Yue, Y.; Liu, J.; Zhang, W.; Yang, X.; Chen, H.; Bi, E.; Ashraful, I.; Gratzel, M.; Han, L. Efficient and Stable Large-Area Perovskite Solar Cells with Inorganic Charge Extraction Layers. *Science* **2015**, *350* (6263), 944−948.

(7) Park, N. G. Research Direction toward Scalable, Stable, and High Efficiency Perovskite Solar Cells. *Adv. Energy Mater.* **2020**, *10* (13), 1903106.

(8) Ban, M.; Zou, Y.; Rivett, J. P. H.; Yang, Y.; Thomas, T. H.; Tan, Y.; Song, T.; Gao, X.; Credgington, D.; Deschler, F.; Sirringhaus, H.; Sun, B. Solution-Processed Perovskite Light Emitting Diodes with Efficiency Exceeding 15% through Additive-Controlled Nanostructure Tailoring. *Nat. Commun.* **2018**, *9* (1), 3892.

(9) Cong, S.; Zou, G.; Lou, Y.; Yang, H.; Su, Y.; Zhao, J.; Zhang, C.; Ma, P.; Lu, Z.; Fan, H.; Huang, Z. Fabrication of Nickel Oxide Nanopillar Arrays on Flexible Electrodes for Highly Efficient Perovskite Solar Cells. *Nano Lett.* **2019**, *19* (6), 3676−3683.

(10) Gao, L.; Quan, L. N.; García de Arquer, F. P.; Zhao, Y.; Munir, R.; Proppe, A.; Quintero-Bermudez, R.; Zou, C.; Yang, Z.; Saidaminov, M. I.; Voznyy, O.; Kinge, S.; Lu, Z.; Kelley, S. O.; Amassian, A.; Tang, J.; Sargent, E. H. Efficient Near-infrared Light-emitting Diodes Based on Quantum Dots in Layered Perovskite. *Nat. Photonics* **2020**, *14* (4), 227−233.

(11) Li, Z.; Hofman, E.; Davis, A. H.; Khammang, A.; Wright, J. T.; Dzikovski, B.; Meulenberg, R. W.; Zheng, W. Complete Dopant Substitution by Spinodal Decomposition in Mn-Doped Two-Dimensional $CsPbCl_3$ Nanoplatelets. *Chem. Mater.* **2018**, *30* (18), 6400−6409.

(12) Lin, K.; Xing, J.; Quan, L. N.; de Arquer, F. P. G.; Gong, X.; Lu, J.; Xie, L.; Zhao, W.; Zhang, D.; Yan, C.; Li, W.; Liu, X.; Lu, Y.; Kirman, J.; Sargent, E. H.; Xiong, Q.; Wei, Z. Perovskite Light-

Emitting Diodes with External Quantum Efficiency Exceeding 20%. *Nature* **2018**, *562* (7726), 245−248.
(13) Wang, S.; Du, L.; Jin, Z.; Xin, Y.; Mattoussi, H. Enhanced Stabilization and Easy Phase Transfer of $CsPbBr_3$ Perovskite Quantum Dots Promoted by High-Affinity Polyzwitterionic Ligands. *J. Am. Chem. Soc.* **2020**, *142* (29F), 12669−12680.
(14) Li, Q.; Wang, Y.; Pan, W.; Yang, W.; Zou, B.; Tang, J.; Quan, Z. High-Pressure Band-Gap Engineering in Lead-Free Cs_2 $AgBiBr_6$ Double Perovskite. *Angew. Chem., Int. Ed.* **2017**, *56* (50), 15969−15973.
(15) Zhou, Q.; Bai, Z.; Lu, W. G.; Wang, Y.; Zou, B.; Zhong, H. In Situ Fabrication of Halide Perovskite Nanocrystal-Embedded Polymer Composite Films with Enhanced Photoluminescence for Display Backlights. *Adv. Mater.* **2016**, *28* (41), 9163−9168.
(16) Abdel-Latif, K.; Epps, R. W.; Kerr, C. B.; Papa, C. M.; Castellano, F. N.; Abolhasani, M. Facile Room-Temperature Anion Exchange Reactions of Inorganic Perovskite Quantum Dots Enabled by a Modular Microfluidic Platform. *Adv. Funct. Mater.* **2019**, *29* (23), 1900712.
(17) Qin, X.; Zhao, Z.; Wang, Y.; Wu, J.; Jiang, Q.; You, J. Recent Progress in Stability of Perovskite Solar Cells. *J. Semicond.* **2017**, *38* (1), 011002.
(18) Babayigit, A.; Ethirajan, A.; Muller, M.; Conings, B. Toxicity of Organometal Halide Perovskite Solar Cells. *Nat. Mater.* **2016**, *15* (3), 247−251.
(19) Zhang, Y.; Yin, J.; Parida, M. R.; Ahmed, G. H.; Pan, J.; Bakr, O. M.; Bredas, J. L.; Mohammed, O. F. Direct-Indirect Nature of the Bandgap in Lead-Free Perovskite Nanocrystals. *J. Phys. Chem. Lett.* **2017**, *8* (14), 3173−3177.
(20) Du, K. Z.; Meng, W.; Wang, X.; Yan, Y.; Mitzi, D. B. Bandgap Engineering of Lead-Free Double Perovskite $Cs_2AgBiBr_6$ through Trivalent Metal Alloying. *Angew. Chem., Int. Ed.* **2017**, *56* (28), 8158−8162.
(21) Slavney, A. H.; Hu, T.; Lindenberg, A. M.; Karunadasa, H. I. A Bismuth-Halide Double Perovskite with Long Carrier Recombination Lifetime for Photovoltaic Applications. *J. Am. Chem. Soc.* **2016**, *138* (7), 2138−2141.
(22) Zhang, J.; Yang, Y.; Deng, H.; Farooq, U.; Yang, X.; Khan, J.; Tang, J.; Song, H. High Quantum Yield Blue Emission from Lead-Free Inorganic Antimony Halide Perovskite Colloidal Quantum Dots. *ACS Nano* **2017**, *11* (9), 9294−9302.
(23) Jellicoe, T. C.; Richter, J. M.; Glass, H. F.; Tabachnyk, M.; Brady, R.; Dutton, S. E.; Rao, A.; Friend, R. H.; Credgington, D.; Greenham, N. C.; Bohm, M. L. Synthesis and Optical Properties of Lead-Free Cesium Tin Halide Perovskite Nanocrystals. *J. Am. Chem. Soc.* **2016**, *138* (9), 2941−2944.
(24) Cai, T.; Shi, W.; Hwang, S.; Kobbekaduwa, K.; Nagaoka, Y.; Yang, H.; Hills-Kimball, K.; Zhu, H.; Wang, J.; Wang, Z.; Liu, Y.; Su, D.; Gao, J.; Chen, O. Lead-Free $Cs_4CuSb_2Cl_{12}$ Layered Double Perovskite Nanocrystals. *J. Am. Chem. Soc.* **2020**, *142* (27), 11927−11936.
(25) Creutz, S. E.; Crites, E. N.; De Siena, M. C.; Gamelin, D. R. Colloidal Nanocrystals of Lead-Free Double-Perovskite (Elpasolite) Semiconductors: Synthesis and Anion Exchange to Access New Materials. *Nano Lett.* **2018**, *18* (2), 1118−1123.
(26) Locardi, F.; Cirignano, M.; Baranov, D.; Dang, Z.; Prato, M.; Drago, F.; Ferretti, M.; Pinchetti, V.; Fanciulli, M.; Brovelli, S.; De Trizio, L.; Manna, L. Colloidal Synthesis of Double Perovskite $Cs_2AgInCl_6$ and Mn-Doped $Cs_2AgInCl_6$ Nanocrystals. *J. Am. Chem. Soc.* **2018**, *140* (40), 12989−12995.
(27) Greul, E.; Petrus, M. L.; Binek, A.; Docampo, P.; Bein, T. Highly Stable, Phase Pure $Cs_2AgBiBr_6$ Double Perovskite Thin Films for Optoelectronic Applications. *J. Mater. Chem. A* **2017**, *5* (37), 19972−19981.
(28) Yang, B.; Chen, J.; Yang, S.; Hong, F.; Sun, L.; Han, P.; Pullerits, T.; Deng, W.; Han, K. Lead-Free Silver-Bismuth Halide Double Perovskite Nanocrystals. *Angew. Chem., Int. Ed.* **2018**, *57* (19), 5359−5363.
(29) Bekenstein, Y.; Dahl, J. C.; Huang, J.; Osowiecki, W. T.; Swabeck, J. K.; Chan, E. M.; Yang, P.; Alivisatos, A. P. The Making and Breaking of Lead-Free Double Perovskite Nanocrystals of Cesium Silver-Bismuth Halide Compositions. *Nano Lett.* **2018**, *18* (6), 3502−3508.
(30) Zhao, X. G.; Yang, J. H.; Fu, Y.; Yang, D.; Xu, Q.; Yu, L.; Wei, S. H.; Zhang, L. Design of Lead-Free Inorganic Halide Perovskites for Solar Cells via Cation-Transmutation. *J. Am. Chem. Soc.* **2017**, *139* (7), 2630−2638.
(31) Dahl, J. C.; Osowiecki, W. T.; Cai, Y.; Swabeck, J. K.; Bekenstein, Y.; Asta, M.; Chan, E. M.; Alivisatos, A. P. Probing the Stability and Band Gaps of $Cs_2AgInCl_6$ and $Cs_2AgSbCl_6$ Lead-Free Double Perovskite Nanocrystals. *Chem. Mater.* **2019**, *31* (9), 3134−3143.
(32) Volonakis, G.; Haghighirad, A. A.; Milot, R. L.; Sio, W. H.; Filip, M. R.; Wenger, B.; Johnston, M. B.; Herz, L. M.; Snaith, H. J.; Giustino, F. $Cs_2InAgCl_6$: A New Lead-Free Halide Double Perovskite with Direct Band Gap. *J. Phys. Chem. Lett.* **2017**, *8* (4), 772−778.
(33) Zhang, Y.; Shah, T.; Deepak, F. L.; Korgel, B. A. Surface Science and Colloidal Stability of Double-Perovskite $Cs_2AgBiBr_6$ Nanocrystals and Their Superlattices. *Chem. Mater.* **2019**, *31* (19), 7962−7969.
(34) Luo, J.; Wang, X.; Li, S.; Liu, J.; Guo, Y.; Niu, G.; Yao, L.; Fu, Y.; Gao, L.; Dong, Q.; Zhao, C.; Leng, M.; Ma, F.; Liang, W.; Wang, L.; Jin, S.; Han, J.; Zhang, L.; Etheridge, J.; Wang, J.; Yan, Y.; Sargent, E. H.; Tang, J. Efficient and Stable Emission of Warm-White Light from Lead-Free Halide Double Perovskites. *Nature* **2018**, *563* (7732), 541−545.
(35) Pan, W. C.; Wu, H. D.; Luo, J. J.; Deng, Z. Z.; Ge, C.; Chen, C.; Jiang, X. W.; Yin, W. J.; Niu, G. D.; Zhu, L. J.; Yin, L. X.; Zhou, Y.; Xie, Q. G.; Ke, X. X.; Sui, M. L.; Tang, J. $Cs_2AgBiBr_6$ Single-Crystal X-ray Detectors with a Low Detection Limit. *Nat. Photonics* **2017**, *11* (11), 726−732.
(36) Luo, J.; Li, S.; Wu, H.; Zhou, Y.; Li, Y.; Liu, J.; Li, J.; Li, K.; Yi, F.; Niu, G.; Tang, J. $Cs_2AgInCl_6$ Double Perovskite Single Crystals: Parity Forbidden Transitions and Their Application for Sensitive and Fast UV Photodetectors. *ACS Photonics* **2018**, *5* (2), 398−405.
(37) Zhou, L.; Xu, Y. F.; Chen, B. X.; Kuang, D. B.; Su, C. Y. Synthesis and Photocatalytic Application of Stable Lead-Free $Cs_2AgBiBr_6$ Perovskite Nanocrystals. *Small* **2018**, *14* (11), 1703762.
(38) Tan, Z.; Li, J.; Zhang, C.; Li, Z.; Hu, Q.; Xiao, Z.; Kamiya, T.; Hosono, H.; Niu, G.; Lifshitz, E.; Cheng, Y.; Tang, J. Highly Efficient Blue-Emitting Bi-Doped Cs_2SnCl_6 Perovskite Variant: Photoluminescence Induced by Impurity Doping. *Adv. Funct. Mater.* **2018**, *28* (29), 1801131.
(39) Chen, N.; Cai, T.; Li, W.; Hills-Kimball, K.; Yang, H.; Que, M.; Nagaoka, Y.; Liu, Z.; Yang, D.; Dong, A.; Xu, C. Y.; Zia, R.; Chen, O. Yb- and Mn-Doped Lead-Free Double Perovskite Cs_2AgBiX_6 (X = Cl^-, Br^-) Nanocrystals. *ACS Appl. Mater. Interfaces* **2019**, *11* (18), 16855−16863.
(40) Liu, Y.; Rong, X.; Li, M.; Molokeev, M. S.; Zhao, J.; Xia, Z. Incorporating Rare-Earth Terbium(III) Ions into $Cs_2AgInCl_6$: Bi Nanocrystals toward Tunable Photoluminescence. *Angew. Chem., Int. Ed.* **2020**, *59* (28), 11634−11640.
(41) Peng, L.; Dutta, A.; Xie, R.; Yang, W.; Pradhan, N. Dot-Wire-Platelet-Cube: Step Growth and Structural Transformations in $CsPbBr_3$ Perovskite Nanocrystals. *ACS Energy Lett.* **2018**, *3* (8), 2014−2020.
(42) Voiry, D.; Shin, H. S.; Loh, K. P.; Chhowalla, M. Low-Dimensional Catalysts for Hydrogen Evolution and CO_2 Reduction. *Nat. Rev. Chem.* **2018**, *2* (1), 0105.
(43) Yang, D.; Li, P.; Zou, Y.; Cao, M.; Hu, H.; Zhong, Q.; Hu, J.; Sun, B.; Duhm, S.; Xu, Y.; Zhang, Q. Interfacial Synthesis of Monodisperse $CsPbBr_3$ Nanorods with Tunable Aspect Ratio and Clean Surface for Efficient Light-Emitting Diode Applications. *Chem. Mater.* **2019**, *31* (5), 1575−1583.
(44) Tong, Y.; Bohn, B. J.; Bladt, E.; Wang, K.; Muller-Buschbaum, P.; Bals, S.; Urban, A. S.; Polavarapu, L.; Feldmann, J. From Precursor Powders to $CsPbX_3$ Perovskite Nanowires: One-Pot Synthesis,

https://dx.doi.org/10.1021/acs.nanolett.0c04148
Nano Lett. 2021, 21, 1620−1627

Growth Mechanism, and Oriented Self-Assembly. *Angew. Chem., Int. Ed.* **2017**, *56* (44), 13887−13892.
(45) Wang, C.; Zhang, Y.; Wang, A.; Wang, Q.; Tang, H.; Shen, W.; Li, Z.; Deng, Z. Controlled Synthesis of Composition Tunable Formamidinium Cesium Double Cation Lead Halide Perovskite Nanowires and Nanosheets with Improved Stability. *Chem. Mater.* **2017**, *29* (5), 2157−2166.
(46) Protesescu, L.; Yakunin, S.; Bodnarchuk, M. I.; Krieg, F.; Caputo, R.; Hendon, C. H.; Yang, R. X.; Walsh, A.; Kovalenko, M. V. Nanocrystals of Cesium Lead Halide Perovskites ($CsPbX_3$, X = Cl, Br, and I): Novel Optoelectronic Materials Showing Bright Emission with Wide Color Gamut. *Nano Lett.* **2015**, *15* (6), 3692−3696.
(47) Dutta, A.; Dutta, S. K.; Das Adhikari, S.; Pradhan, N. Tuning the Size of $CsPbBr_3$ Nanocrystals: All at One Constant Temperature. *ACS Energy Lett.* **2018**, *3* (2), 329−334.
(48) Zhang, D.; Yang, Y.; Bekenstein, Y.; Yu, Y.; Gibson, N. A.; Wong, A. B.; Eaton, S. W.; Kornienko, N.; Kong, Q.; Lai, M.; Alivisatos, A. P.; Leone, S. R.; Yang, P. Synthesis of Composition Tunable and Highly Luminescent Cesium Lead Halide Nanowires through Anion-Exchange Reactions. *J. Am. Chem. Soc.* **2016**, *138* (23), 7236−7239.
(49) Pan, A.; He, B.; Fan, X.; Liu, Z.; Urban, J. J.; Alivisatos, A. P.; He, L.; Liu, Y. Insight into the Ligand-Mediated Synthesis of Colloidal $CsPbBr_3$ Perovskite Nanocrystals: The Role of Organic Acid, Base, and Cesium Precursors. *ACS Nano* **2016**, *10* (8), 7943−54.
(50) Dang, Z.; Dhanabalan, B.; Castelli, A.; Dhall, R.; Bustillo, K. C.; Marchelli, D.; Spirito, D.; Petralanda, U.; Shamsi, J.; Manna, L.; Krahne, R.; Arciniegas, M. P. Temperature-Driven Transformation of $CsPbBr_3$ Nanoplatelets into Mosaic Nanotiles in Solution through Self-Assembly. *Nano Lett.* **2020**, *20* (3), 1808−1818.
(51) Shamsi, J.; Dang, Z.; Bianchini, P.; Canale, C.; Di Stasio, F.; Brescia, R.; Prato, M.; Manna, L. Colloidal Synthesis of Quantum Confined Single Crystal $CsPbBr_3$ Nanosheets with Lateral Size Control up to the Micrometer Range. *J. Am. Chem. Soc.* **2016**, *138* (23), 7240−7243.
(52) Butler, S. Z.; Hollen, S. M.; Cao, L.; Cui, Y.; Gupta, J. A.; Gutierrez, H. R.; Heinz, T. F.; Hong, S. S.; Huang, J.; Ismach, A. F.; Johnston-Halperin, E.; Kuno, M.; Plashnitsa, V. V.; Robinson, R. D.; Ruoff, R. S.; Salahuddin, S.; Shan, J.; Shi, L.; Spencer, M. G.; Terrones, M.; Windl, W.; Goldberger, J. E. Progress, Challenges, and Opportunities in Two-Dimensional Materials Beyond Graphene. *ACS Nano* **2013**, *7* (4), 2898−926.
(53) Mohiuddin, M.; Zavabeti, A.; Haque, F.; Mahmood, A.; Datta, R.; Syed, N.; Khan, M. W.; Jannat, A.; Messalea, K.; Zhang, B.; Chen, G.; Zhang, H.; Ou, J. Z.; Mahmood, N. Synthesis of Two-Dimensional Hematite and Iron Phosphide for Hydrogen Evaluation. *J. Mater. Chem. A* **2020**, *8* (5), 2789−2797.
(54) Jin, H.; Guo, C.; Liu, X.; Liu, J.; Vasileff, A.; Jiao, Y.; Zheng, Y.; Qiao, S. Z. Emerging Two-Dimensional Nanomaterials for Electrocatalysis. *Chem. Rev.* **2018**, *118* (13), 6337−6408.
(55) Low, J.; Cao, S.; Yu, J.; Wageh, S. Two-Dimensional Layered Composite Photocatalysts. *Chem. Commun.* **2014**, *50* (74), 10768−10777.
(56) Su, T.; Shao, Q.; Qin, Z.; Guo, Z.; Wu, Z. Role of Interfaces in Two-Dimensional Photocatalyst for Water Splitting. *ACS Catal.* **2018**, *8* (3), 2253−2276.
(57) Connor, B. A.; Leppert, L.; Smith, M. D.; Neaton, J. B.; Karunadasa, H. I. Layered Halide Double Perovskites: Dimensional Reduction of $Cs_2AgBiBr_6$. *J. Am. Chem. Soc.* **2018**, *140* (15), 5235−5240.
(58) Li, S.; Luo, J.; Liu, J.; Tang, J. Self-Trapped Excitons in All-Inorganic Halide Perovskites: Fundamentals, Status, and Potential Applications. *J. Phys. Chem. Lett.* **2019**, *10* (8), 1999−2007.
(59) Zelewski, S. J.; Urban, J. M.; Surrente, A.; Maude, D. K.; Kuc, A.; Schade, L.; Johnson, R. D.; Dollmann, M.; Nayak, P. K.; Snaith, H. J.; Radaelli, P.; Kudrawiec, R.; Nicholas, R. J.; Plochocka, P.; Baranowski, M. Revealing the Nature of Photoluminescence Emission in the Metal-Halide Double Perovskite $Cs_2AgBiBr_6$. *J. Mater. Chem. C* **2019**, *7* (27), 8350−8356.
(60) Schade, L.; Wright, A. D.; Johnson, R. D.; Dollmann, M.; Wenger, B.; Nayak, P. K.; Prabhakaran, D.; Herz, L. M.; Nicholas, R.; Snaith, H. J.; Radaelli, P. G. Structural and Optical Properties of $Cs_2AgBiBr_6$ Double Perovskite. *ACS Energy Lett.* **2019**, *4* (1), 299−305.
(61) Zhu, H.; Fan, Z.; Yu, L.; Wilson, M. A.; Nagaoka, Y.; Eggert, D.; Cao, C.; Liu, Y.; Wei, Z.; Wang, X.; He, J.; Zhao, J.; Li, R.; Wang, Z.; Grunwald, M.; Chen, O. Controlling Nanoparticle Orientations in the Self-Assembly of Patchy Quantum Dot-Gold Heterostructural Nanocrystals. *J. Am. Chem. Soc.* **2019**, *141* (14), 6013−6021.
(62) Holder, C. F.; Schaak, R. E. Tutorial on Powder X-ray Diffraction for Characterizing Nanoscale Materials. *ACS Nano* **2019**, *13* (7), 7359−7365.
(63) Yang, H.; Cai, T.; Liu, E.; Hills-Kimball, K.; Gao, J.; Chen, O. Synthesis and Transformation of Zero-Dimensional Cs_3BiX_6 (X = Cl, Br) Perovskite-Analogue Nanocrystals. *Nano Res.* **2020**, *13* (1), 282−291.
(64) Creutz, S. E.; Liu, H.; Kaiser, M. E.; Li, X.; Gamelin, D. R. Structural Diversity in Cesium Bismuth Halide Nanocrystals. *Chem. Mater.* **2019**, *31* (13), 4685−4697.
(65) Lee, W.; Choi, D.; Kim, S. Colloidal Synthesis of Shape-Controlled Cs_2NaBiX_6 (X = Cl, Br) Double Perovskite Nanocrystals: Discrete Optical Transition by Non-Bonding Characters and Energy Transfer to Mn Dopants. *Chem. Mater.* **2020**, *32* (16), 6864−6874.
(66) Nie, S.; Emory, S. R. Probing Single Molecules and Single Nanoparticles by Surface-Enhanced Raman Scattering. *Science* **1997**, *275* (5303), 1102−1106.
(67) Peng, L.; Dutta, S. K.; Mondal, D.; Hudait, B.; Shyamal, S.; Xie, R.; Mahadevan, P.; Pradhan, N. Arms Growth and Facets Modulation in Perovskite Nanocrystals. *J. Am. Chem. Soc.* **2019**, *141* (40), 16160−16168.
(68) Weidman, M. C.; Seitz, M.; Stranks, S. D.; Tisdale, W. A. Highly Tunable Colloidal Perovskite Nanoplatelets through Variable Cation, Metal, and Halide Composition. *ACS Nano* **2016**, *10* (8), 7830−7839.
(69) Yang, B.; Chen, J.; Hong, F.; Mao, X.; Zheng, K.; Yang, S.; Li, Y.; Pullerits, T.; Deng, W.; Han, K. Lead-Free, Air-Stable All-Inorganic Cesium Bismuth Halide Perovskite Nanocrystals. *Angew. Chem., Int. Ed.* **2017**, *56* (41), 12471−12475.
(70) Xu, Y. F.; Yang, M. Z.; Chen, B. X.; Wang, X. D.; Chen, H. Y.; Kuang, D. B.; Su, C. Y. A $CsPbBr_3$ Perovskite Quantum Dot/Graphene Oxide Composite for Photocatalytic CO_2 Reduction. *J. Am. Chem. Soc.* **2017**, *139* (16), 5660−5663.
(71) Barbagiovanni, E. G.; Lockwood, D. J.; Simpson, P. J.; Goncharova, L. V. Quantum Confinement in Si and Ge Nanostructures: Theory and Experiment. *Appl. Phys. Rev.* **2014**, *1* (1), 011302.
(72) Zhang, G.; Chaves, A.; Huang, S.; Wang, F.; Xing, Q.; Low, T.; Yan, H. Determination of Layer-Dependent Exciton Binding Energies in Few-Layer Black Phosphorus. *Sci. Adv.* **2018**, *4* (3), No. eaap9977.
(73) Zheng, K.; Zhu, Q.; Abdellah, M.; Messing, M. E.; Zhang, W.; Generalov, A.; Niu, Y.; Ribaud, L.; Canton, S. E.; Pullerits, T. Exciton Binding Energy and the Nature of Emissive States in Organometal Halide Perovskites. *J. Phys. Chem. Lett.* **2015**, *6* (15), 2969−2975.
(74) Otterburg, T.; Oberli, D. Y.; Dupertuis, M. A.; Moret, N.; Pelucchi, E.; Dwir, B.; Leifer, K.; Kapon, E. Enhancement of the Binding Energy of Charged Excitons in Disordered Quantum Wires. *Phys. Rev. B: Condens. Matter Mater. Phys.* **2005**, *71* (3), 033301.

https://dx.doi.org/10.1021/acs.nanolett.0c04148
Nano Lett. 2021, 21, 1620−1627